Enhanced hydrothermal activity on an ultraslow-spreading supersegment with a seismically detected melting anomaly

Huaiming Li[a*], Chunhui Tao[a*], Xihe Yue[a,b], Edward T Baker[c], Xianming Deng[a], Jianping Zhou[a,d], Yuan Wang[a], Guoyin Zhang[a], Jie Chen[e], Shihui Lü[d], Xin Su[d]

[a] Key Laboratory of Submarine Geosciences, Second Institute of Oceanography, Ministry of Natural Resources, Hangzhou, China

[b] College of Marine Science and Technology, China University of Geosciences, Wuhan, China

[c] NOAA Pacific Marine Environmental Laboratory, Seattle, WA, USA

[d] School of Ocean Sciences, China University of Geosciences, Beijing, China

[e] Equipe de Géosciences Marines, Institut de Physique du Globe de Paris, Université de Paris, Paris, France

* Corresponding author: huaiming_lee@163.com；taochunhuimail@163.com

Highlights:

1. Site frequency is 3× higher than predicted by the global trend for ultraslow OSRs.
2. Increased hydrothermal activity is related to a melting anomaly.
3. Active site distribution implies magmatic heat sources beyond the known melt body.

Abstract: Seafloor hydrothermal venting fields occur on all ocean spreading ridges (OSRs) regardless of spreading rates. However, the distribution of seafloor hydrothermal activity such as frequency and spacing on ultraslow-spreading OSRs are poorly known. Chinese Dayang cruises from 2015 to 2016 conducted detailed water column surveys for seafloor hydrothermal activity using a towed system, with an array of turbidity sensors and a near-bottom camera, along the ultraslow-spreading Southwest Indian Ridge. Here we report the discovery of multiple hydrothermal plumes overlying segments 28, 29, and 30 between the Indomed and Gallieni fracture zones. From these data, and earlier explorations in segments 25-27, we identify nine active venting sites. The spatial density (F_s, sites/100 km) of active sites along the 394 km of ridge axis in our study area is thus 2.8, nearly 3× higher than predicted by the global trend of F_s for ultraslow OSRs in the InterRidge database. Previous studies concluded that an enhanced magma supply to the central Indomed–Gallieni supersegment 11-8 Ma is now limited to segment 27. Our results indicate that although hydrothermal activity may be most concentrated in segment 27, the discoveries of active venting in segments 25-30 implies the presence of additional magma bodies across a broad extent of the Indomed–Gallieni supersegment.

Keywords: Seafloor hydrothermal activity; Tectonic and magmatic activity; Mantle fertility; Ultraslow-spreading ridge; Southwest Indian Ridge

1. Introduction

Nearly four decades of surveying seafloor hydrothermal activity has resulted in the discovery of about 507 confirmed (visually) or inferred (from water column observations) hydrothermal venting fields along ocean spreading ridges (OSRs) (http://vents-data.interridge.org; Tao et al., 2012; Beaulieu et al., 2015; German et al., 2016; Baker, 2017). There is a global trend between the spatial frequency of hydrothermal venting fields (F_S, sites/100 km) and the full spreading rate of OSRs, which is considered to reflect the long-term magmatic budget (Baker et al., 1996; Baker and German, 2004; Baker, 2017). According to this model, about 800 hydrothermal venting fields remain to be found, and nearly 450 of these will be on slow- (20-55 mm/a) and ultraslow- (<20 mm/a) spreading OSRs (Beaulieu et al., 2015).

Magmatic activity and tectonically generated permeability are regarded as two vital geological processes controlling seafloor hydrothermal activity along OSRs (e.g., Baker et al., 2004; German et al., 2016; German and Parson, 1998; Son et al., 2014). High-temperature hydrothermal venting driven by an axial (or near-axial) magma chamber, generally associated with axial volcanic ridges, has been found on segments of fast, intermediate, slow, and ultraslow OSRs (Gente et al., 1991; Allerton et al., 1995; Ondréas et al., 1997; Baker, 2009; Haase et al., 2007, 2009; Marcon et al., 2013; Yue et al., 2019). In contrast to magmatically controlled hydrothermal activity on fast- and intermediate-rate OSRs, the location of many vent fields along slow and ultraslow OSRs are controlled by tectonic activity, typically on non-transform offsets and ridge valley walls above an axial volcanic ridge (Demartin et al., 2007; Tao et al., 2012; German et al., 2016). In these areas, long-lived, downward-dipping faults provide pathways for hydrothermal fluid flow (McCaig et al., 2007, 2010; German et al., 2016; Zhao et al., 2013). Although mantle upwelling and crustal cooling provide heat along slow-spreading OSRs (Canales et al., 2007; Escartín et al., 2008), magma sources are necessary for long-lived, high-temperature hydrothermal venting (Lowell, 2010).

In the past two decades, nearly half of the systematic survey efforts for hydrothermal activity have been conducted along slow-spreading OSRs, whereas the fewest occurred on ultraslow OSRs (Beaulieu et al., 2015). China Ocean Mineral Resources Research & Development Association conducted China Dayang Cruises (CDC) #34 and #39 in 2016 and 2017, in order to investigate seafloor hydrothermal activity on segments 27, 28, 29 and 30 along the Southwest Indian Ridge between the Indomed and Gallieni fracture zones. The cruises were related to a contract between the China Ocean Mineral Resources Research & Development Association and the International Seabed Authority for polymetallic sulphides exploration (Fig. 1). The study area has two intriguing aspects for seafloor hydrothermal activity: ultraslow spreading and areas of unusually thick crust (up to ~10 km) suggestive of a local melting anomaly. Here we report the discovery of multiple hydrothermal plumes and discuss the implications in terms of variable magma sources to an ultraslow-spreading ridge.

2. **Geological setting**

The Southwest Indian Ridge, extending ~7700 km between the Rodriguez and Bouvet triple junctions, is an ultraslow-spreading ridge with a full spreading rate of 12.2–14.5 mm/a (DeMets et al., 2015) (Fig. 1). Our study area on the central Southwest Indian Ridge is a first-order supersegment from 46°E to 52°20'E, between the Indomed and Gallieni fracture zones. The position of the mid-ocean ridge axis corresponds to the center of present magmatic or tectonic activity (Mendel et al., 1997; Macdonald, 1998; Cannat et al., 1999). Second-order segments on the Indomed–Gallieni supersegment are numbered 25-32 from east to west (Cannat et al., 1999) (Fig.2).

An apparent increase in magma supply occurred suddenly between 11 and 8 Ma along the central portion of the supersegment (Sauter et al., 2009; Yang et al., 2017; Yu and Dick, 2020). The shallowest depth of the supersegment axis is ~1650 m on segment 27, one of the two shallowest ridge segments on the Southwest Indian Ridge (Zhang et al., 2013). Seismic studies suggest the melting anomaly is currently centered in segment 27, with a smaller anomaly possibly present in segment 28. The 9.5-km-thick crust revealed by seismic data along- and off-axis at segment 27 suggests that intense magmatism lasted at least 3 Ma (Zhang et al., 2013; Li et al., 2015). An asymmetric seafloor fabric and dome-like topography have been observed on segment 28 (Zhao et al., 2013), where the crustal thickness is ~5 km (Niu et al., 2015; Li et al., 2015). Three hydrothermal venting fields have been previously reported in our study area, including the inactive field Duanqiao in segment 27, and the active fields Longqi in segment 28 and Yuhuang in segment 29 (Han et al., 2010; Tao et al., 2012) (Figs. 1, 2). Additionally, two inferred hydrothermal venting fields were reported in segment 25 and 26 (Tao et al., 2009).

3. **Data and methods**

The topographic map in this study was drawn using the bathymetry data with a grid of 50-m intervals, acquired during cruises of the R/V Dayang Yihao and the R/V Xiangyanghong 10 from 2008 to 2016, using a Simrad EM120 multibeam system that operated with a source frequency of 12 kHz (Fig. 2).

Based on bathymetric analyses of the study area, we selected survey areas covering ~6000 km^2 for exploration during the first and second legs of China Dayang cruise (CDC) 34 in 2015 and the first leg of China Dayang cruise 39 in 2016. Nearly half of the areas were surveyed using a deep-tow hydrothermal detection system (DHDS) with a line spacing of 2–4 km on segments 27-30. Yue et al. (2019) reported the results of DHDS survey on segment 27, and results from segments 28-30 are presented here.

The DHDS includes a deep-tow body with video, still cameras, and an Oxidation-Reduction Potential (ORP) sensor on some tows, as well as 3 to 4 Miniature Autonomous Plume Recorders along the cable within 300 m of the deep-tow body. During a DHDS survey, we aimed to keep the deep-tow body 3–5 m above the seafloor in order to collect seabed images, although micro-topographical variability occasionally caused contact with the seafloor and resuspension of sediment.

The voltage output of Miniature Autonomous Plume Recorders is equivalent to nephelometric turbidity units (NTU). We cleaned the data by removing points laying outside +/- 3 standard deviations in 50-point data blocks. We then smoothed the remaining data using a 5-point (25 s) moving average. Lastly, we calculated a △NTU value by subtracting a background value for each Miniature Autonomous Plume Recorder based on the NTU value of water above plume depth during each tow.

ORP sensors detect dissolved chemical species (e.g., Fe^{+2}, HS^-, H_2 (Walker et al., 2007; Resing et al., 2009)) from all vent types, including low-temperature vents with little or no ΔNTU signature. ORP sensors respond immediately, with decreasing potential values (mV), and the signal dissipates within ~ 1 km from the source. This results in a more precise location of a source than is possible with optical sensors (Baker et al., 2016, 2017).

4. Results

4.1 Segment 28

Segment 28 is 42 km long, with an axial volcanic ridge having a width of 5 km and an across-axis relief of 500 m (Fig. 3). The shallowest axial water depth, 2740 m, is located at 49°46'E. The water depth deepens eastward to 3390 m and westward to 3840 m. Segment 28 presents a highly asymmetric topography. The southern ridge flank is relatively shallow (<2000 m) and locally bears corrugations typical of oceanic core complex. The northern ridge flank has a deeper topography (>2000 m). DHDS survey lines were carried out in a 900 km^2 area, covering nearly all the southern and part of the northern ridge flanks (Fig. 3). Longqi, regarded as the first confirmed active hydrothermal field on an ultraslow spreading ridge (Tao et al., 2012), is located on the southeast wall of the segment 28 axial valley (Zhao et al., 2013; Tao et al. 2014).

Increased ΔNTU values define a broad and thick hydrothermal plume between ~2500 and 2700 m on the westward dipping axial valley wall of segment 28, ~12 km southwest of Longqi (Fig. 4a). The plume extends about 4 km along the survey line and is >200 m thick. A ΔNTU maximum of 0.06 was detected at 2600 m (Fig. 4b). An ORP sensor was mounted on the tow body during this tow, and recorded two prominent anomalies at 37°52.4’ and 37°52.8’S, identified by sharp drops in ORP (mV) followed by a characteristic slow recovery (tow direction was southward). We thus infer that one or more active discharge sites occur in a hydrothermal field we refer to as Longqi-2. The most likely location is near 49°32′E/37°52.8′S at a depth of ~2700 m, where the largest ORP anomaly and a near-bottom ΔNTU anomaly occur. Maximum ΔNTU values occur downstream from the maximum ORP anomaly because of the time lag in precipitation of particulate Fe from hydrothermal dissolved Fe (e.g., Field and Sherrell, 2000). The presence of ORP anomalies confirms that the observed optical plume is not sourced at Longqi, even though its depth is similar to that presumed for Longqi-2.

4.2 Segment 29

Segment 29 is 44 km long, featuring a well-defined axial volcanic ridge 4.2 km wide and having an across-axis relief of 300 m (Fig. 5). The shallowest water depth (2760 m) occurs at 49°20'E, deepening eastward to 3840 m and westward to 4040 m. DHDS survey lines were conducted on the southern and northern walls of the axial valley, within an area of ~900 km^2. The Yuhuang field is located on top of a linear swell south of the axial volcanic ridge at a depth of 1300 to 1400 m (Han et al., 2010). Bulk geochemistry, plus sulfur and zinc isotopic compositions of sulfide samples, were analysed by Liao et al. (2018, 2019). A short survey line over the Yuhuang field (Fig. 6a, b) found plume horizons at multiple depths between 1400 and 1800 m, demonstrating that the field was active.

A broad and deeper hydrothermal plume extending ~10 km was detected by a DHDS survey downslope from Yuhuang hydrothermal field (Fig. 7a, b). The ~500-m-thick plume is centered near 2500 m, with a maximum ΔNTU of ~0.03. Hydrothermal venting from the Yuhuang field is too shallow to produce a plume at this depth. We infer that a new hydrothermal vent field, Yuhuang-2, is near the location of the highest plume ΔNTU, 49°13′E/37°56′S, ~3.5 km west from the Yuhuang hydrothermal field.

4.3 Segment 30

Segment 30 is 90 km long and the shallowest water depth is 2760 m, deepening eastward to 4040 m and westward to 3850 m (Fig. 8). DHDS survey lines were in a ~1400 km^2 area. A hydrothermal plume extending ~4-5 km was located at the foot of the southern axial valley wall (Fig. 9a). The maximum ΔNTU anomaly of ~0.04 was centered at ~3000 m (Fig. 9b). Because a ΔNTU anomaly was only detected by the uppermost sensor, the true thickness of the plume and the location of its source are uncertain. We provisionally locate the S30 hydrothermal field at 48°55′E/38°3′S, below the observed plume.

5. Discussion

5.1 Hydrothermal vent spatial frequency (F_s) on ultraslow spreading segments

Our results identified five confirmed or inferred active hydrothermal vent fields on segments 28, 29, and 30. Yue et al. (2019) reported one confirmed, three inferred, and five suspected (because of inconclusive plume data) hydrothermal fields on segment 27; conservatively, we consider here only the four confirmed and inferred fields. In addition, Tao et al. (2009) reported two fields on segments 25 and 26. The total length of actively spreading ridge along segments 25-30 is 394 km (Beaulieu et al., 2015), yielding a F_s value of 2.8. This value is roughly 2× that in the InterRidge database for the 49°-52°E section of the Southwest Indian Ridge (Beaulieu et al., 2015). Perhaps more significantly, our $F_{s,}$ is ~3× that for other studied ultraslow ridges of similar spreading rate, and outside the 95% confidence level predicted for ultraslow ridges based on a global trend of F_s versus the spreading rate for 29 OSRs in the InterRidge database (Fig. 10) (Beaulieu et al., 2015; Baker, 2017). (Note that this trend is based on ridge sections using exploration techniques similar to those in this paper, and does not include the few studies where recent detailed optical and chemical plume surveys have found significantly higher F_s values (see below)).

Importantly, two primary reasons demand that our calculated F_s value must be a minimum estimate of the true value. First, detailed surveys along the entire axial lengths of segments 25-30 have not yet been conducted. Existing DHDS lines were run within ~6000 km^2 of the axial valley and inner flank walls on segments 27-30, only about half of the total area. The axial volcanic ridges of segments 28 and 29 remain unsurveyed, and coverage in segments 25 and 26 is especially sparse. Second, optimal survey techniques were not available. Turbidity sensors on the tow lines covered a water interval of ~300 m, only minimally adequate at depths >~3000 m, and lacked ORP capability (an ORP sensor was on the deep tow body on some tows). Continuous spatial surveys using both ΔNTU and ORP sensors (as used by Yue et al. (2019) on segment 27) find that the number of active vent sites on fast and intermediate-rate OSRs may be at least a factor of 3–6 higher than now presumed by the global trend (Fig. 10) (Baker et al. 2016), and there is no reason to expect a different outcome on slow-rate OSRs. Therefore, the true F_s value in our study area is likely to be substantially higher than our minimum value.

5.2 Magmatic and tectonic control of hydrothermal activity distribution

Excess magmatism in the Indomed–Gallieni supersegment has been recognized for decades (see the discussion in Yu and Dick (2020)) and must contribute to the higher than expected F_s. The source of this magma has been variously attributed to the 1000-km-distant Crozet hotspot (Sauter et al., 2009; Breton et al., 2013; Yang et al., 2017) or to more local magmatic conditions (Meyzen et al., 2005; Dalton et al., 2014). A new petrographic analysis of the Indomed–Gallieni supersegment (Yu and Dick, 2020) finds it an example of regional mantle fertility driven by plate reorganization, not hotspot activity. Whatever the origin of the melting anomaly, it clearly propagated eastward from the Indomed fracture zone from 11 to 8 Ma, dying out at ~1 Ma and apparently leaving segment 27 as a localized remnant (Sauter et al., 2009; Yu and Dick, 2020). This remnant is presently expressed by an axial magma chamber in the lower crust identified by a large low-velocity anomaly ~4–9 km below the seafloor (Zhang et al., 2013; Li et al., 2015). Li et al. (2015) suggest that segment 28 also contains a magmatic center, although the seismic data is insufficient to demonstrate a melt lens as detected in segment 27.

Although segment 27 is presently the most magma-rich location known on the supersegment, the presence of multiple active vent fields in segments to the west is strong evidence that some magmatic heat sources remain undiscovered along the inferred path of the melting anomaly (Sauter et al., 2009; Yu and Dick, 2020). This conclusion is not surprising given the known association of high-temperature venting with the presence of a magma chamber. A compilation of data from six intermediate- to fast-spreading ridge sections (totalling 2100 km length), all of which had been seismically surveyed for the presence of an axial magma chamber, found that high-temperature vent fields were almost universally associated with the presence or inference of magma along those sections (Baker, 2009). This association was given a theoretical basis by Lowell (2010), who used heat flux modelling to show that heat transfer from an actively replenishing subaxial magma chamber is required to maintain high-temperature vent systems on decadal time scales.

Although high-temperature venting in our study area has been visually confirmed only at Longqi, the plume characteristics at the other inferred sites suggest they are also high-temperature and thus powered by magmatic heat. Such sites commonly show plume ΔNTU >~0.1, plume rise >~100 m, and a heat flux >~1 MW (e.g., Germanovich et al., 2015). All the sites discovered here satisfy the first two characteristics, and we can estimate heat fluxes from their plume rise. As described by Germanovich et al. (2015), heat flux $H = (c_p\rho/\alpha g)(z/3.8)^4 N^3$, where c_p is heat capacity for neutrally buoyant plume water at ~300 bar (4200 J/(kg°C)), ρ is the local plume fluid density (1028 kg/m^3), α is the thermal expansion coefficient (~1.3×10^{-4}/°C), g is gravitational acceleration (9.8 m/s^2), z is plume rise (m), and N is the local Brunt-Väisälä frequency ($[(-g/\Delta\rho)(\rho\Delta z)]^{1/2}$, 5.95 $\times 10^{-4}$ Hz). To estimate z we use the inferred depth at site locations shown in Figs. 3, 5, and 8 and measure z from the seafloor to the plume ΔNTU maximum (Figs. 4, 7, and 9). For Longqi-2 and Yuhuang-2, z = 200 m and H = 4.6 MW; and for S30, z = 350 m and H = 43 MW. These are rough estimates of H, especially given the uncertainty of the true vent depths, but they are unlikely to overestimate H by an order of magnitude.

Vent fields in segments 27-30 are found from the near-axis region to the upper flank of the studied axial valleys (Fig. 11). Hydrothermal activity is most concentrated on the axial volcanic ridge of segment 27, consistent with the location of a broad and thick melt body (Yue et al., 2019). These hydrothermal sites are similar to magmatic-hosted hydrothermal sites on the slow-spreading Mid-Atlantic Ridge (Gente et al., 1991; Allerton et al., 1995; Ondréas et al., 1997; Haase et al., 2007, 2009; Marcon et al., 2013). On segments 28, 29, and 30, with deeper axial valleys, asymmetric ridge flanks, and short axial volcanic ridges, known fields occur on the axial valley walls. This distribution is consistent with the importance of normal and detachment faults in channelling hydrothermal fluids to off-axis vent fields (McCaig et al., 2007). These faults may have been activated by the migration of the melting anomaly through our study area, opening additional fluid pathways to the magmatic heat sources. Owing to the paucity of DHDS lines on the ridge axis of the survey segments, however, we cannot preclude the existence of hydrothermal activity on the axial volcanic ridges of those segments.

6. Conclusions

We used detailed water column surveys to detect evidence of seafloor hydrothermal venting on multiple segments of the ultraslow-spreading Southwest Indian Ridge between the Indomed and Gallieni fracture zones. Eleven active fields (three confirmed and eight inferred) occur on the explored segments 25-30, which extend ~394 km along the ridge axis. The spatial density of vent fields (F_s) is thus 2.8 sites/100 km, about 3× higher than expected for an ultraslow ridge based on the InterRidge global dataset of spreading ridges, and 2× greater than found for the same area in that database. We emphasize that our F_s is a minimum value given the present incomplete state of exploration in this area. The distribution of hydrothermal activity is consistent with the confirmed presence of magma bodies beneath segment 27 and inferred for segment 28. The presence of active venting on segments 25-30 implies the presence of additional magma bodies across a broad extent of the Indomed–Gallieni supersegment.

Acknowledgements

We thank the crews of the R/V Dayngyihao and Xiangyanghong 10, and all the science party members of the Dayang cruises 30, 34, 39, 40, and 43. Three reviewers, including H. Dick, provided close scrutiny and valuable improvements to the paper. This is PMEL Contribution 5054.

Funding

This research was funded by the China Ocean Mineral Resources Research and Development Association Program (DY125-11-R-05). NOAA/PMEL provided funding for ETB.

References

Allerton, S., Murton, B.J., Searle, R.C., Jones, M., 1995. Extensional faulting and segmentation of the Mid-Atlantic Ridge north of the Kane Fracture Zone (24° 00′ N to 24° 40′ N). Mar. Geophys. Res. 17, 37–61. https://doi.org/10.1007/BF01268050

Baker, E.T., 2017. Exploring the ocean for hydrothermal venting: New techniques, new discoveries, new insights. Ore Geol. Rev. 86, 55–69.

Baker, E.T., 2009. Relationships between hydrothermal activity and axial magma chamber distribution, depth, and melt content. Geochemistry, Geophys. Geosystems 10, 1–15.

Baker, E.T., Chen, Y.J., Morgan, J.P., 1996. The relationship between near-axis hydrothermal cooling and the spreading rate of mid-ocean ridges. Earth Planet. Sci. Lett. 142, 137–145.

Baker, E.T., Edmonds, H.N., Michael, P.J., Bach, W., Dick, H.J.B., Snow, J.E., Walker, S.L., 2004. Hydrothermal venting in magma deserts: The ultraslow- spreading Gakkel and Southwest Indian Ridges. Geochemistry, Geophys. Geosystems 5, 1–29. https://doi.org/10.1029/2004GC000712

Baker, E.T., German, C.R., 2004. On the Global Distribution of Hydrothermal Vent Fields, in: Mid-Ocean Ridges: Hydrothermal Interactions Between the Lithosphere and Oceans. pp. 245–266.

Baker, E.T., Resing, J.A., Haymon, R.M., Tunnicliffe, V., Lavelle, J.W., Martinez, F., Ferrini, V., Walker, S.L., Nakamura, K., 2016. How many vent fields? New estimates of vent field populations on ocean ridges from precise mapping of hydrothermal discharge locations. Earth Planet. Sci. Lett. 449, 186–196.

Beaulieu, S.E., Baker, E.T., German, C.R., 2015. Where are the undiscovered hydrothermal vents on oceanic spreading ridges? Deep. Res. Part II Top. Stud. Oceanogr. 121, 202–212. https://doi.org/10.1016/j.dsr2.2015.05.001

Canales, J.P., Sohn, R.A., DeMartin, B.J., 2007. Crustal structure of the Trans-Atlantic Geotraverse (TAG) segment (Mid-Atlantic Ridge, 26°10′N): Implications for the nature of hydrothermal circulation and detachment faulting at slow spreading ridges. Geochemistry, Geophys. Geosystems 8. https://doi.org/10.1029/2007GC001629

Cannat, M., Rommevaux-Jestin, C., Sauter, D., Deplus, C. and Mendel, V., 1999. Formation of the axial relief at the very slow spreading Southwest Indian Ridge (49 to 69 E). Journal of Geophysical Research: Solid Earth, 104(B10), pp.22825-22843.

Demartin, B.J., Sohn, R.A., Canales, J.P., Humphris, S.E., 2007. Kinematics and geometry of active detachment faulting beneath the Trans-Atlantic Geotraverse (TAG) hydrothermal field on the Mid-Atlantic Ridge. Geology 35, 711–714.

DeMets, C., Merkouriev, S., Sauter, D., 2015. High-resolution estimates of Southwest Indian Ridge plate motions, 20 Ma to present. Geophys. J. Int. 203, 1495–1527. https://doi.org/10.1093/gji/ggv366.

Escartín, J., Smith, D.K., Cann, J., Schouten, H., Langmuir, C.H., Escrig, S., 2008. Central role of detachment faults in accretion of slow-spreading oceanic lithosphere. Nature 455, 790–794.

Field, M.P. and Sherrell, R.M., 2000. Dissolved and particulate Fe in a hydrothermal plume at 9 45′ N, East Pacific Rise:: Slow Fe (II) oxidation kinetics in Pacific plumes. Geochim, Cosmochim. Acta, 64, 619-628.

Gente, P., Mével, C., Auzende, J.M., Karson, J.A., Fouquet, Y., 1991. An example of a recent accretion on the Mid-Atlantic Ridge: the Snake Pit neovolcanic ridge (MARK area, 23°22′N). Tectonophysics 190, 1–29. https://doi.org/10.1016/0040-1951(91)90352-S.

German, C R, Parson, L.M., 1998. Distributions of hydrothermal activity along the Mid-Atlantic Ridge: interplay of magmatic and tectonic controls. Earth Planet. Sci. Lett. 160, 327–341.

German, C. R., Parson, L.M., 1998. Distributions of hydrothermal activity along the Mid-Atlantic Ridge: interplay of magmatic and tectonic controls. Earth Planet. Sci. Lett. 160, 327–341. https://doi.org/10.1016/S0012-821X(98)00093-4.

German, C.R., Petersen, S., Hannington, M.D., 2016. Hydrothermal exploration of mid-ocean ridges: Where might the largest sulfide deposits be forming? Chem. Geol. 420, 114–126.

Germanovich, L.N., Hurt, R.S., Smith, J.E., Genc, G. and Lowell, R.P., 2015. Measuring fluid flow and heat output in seafloor hydrothermal environments. J. Geophys. Rese., 120, 8031-8055.

Haase, K.M., Koschinsky, A., Petersen, S., Devey, C.W., German, C., Lackschewitz, K.S., Melchert, B., Seifert, R., Borowski, C., Giere, O., Paulick, H., 2009. Diking, young volcanism and diffuse hydrothermal activity on the southern Mid-Atlantic Ridge: The Lilliput field at 9°33′S. Mar. Geol. 266, 52–64. https://doi.org/10.1016/j.margeo.2009.07.012.

Haase, K.M., Petersen, S., Koschinsky, A., Seifert, R., Devey, C.W., Keir, R., Lackschewitz, K.S., Melchert, B., Perner, M., Schmale, O., Süling, J., Dubilier, N., Zielinski, F., Fretzdorff, S., Garbe-Schönberg, D., Westernströer, U., German, C.R., Shank, T.M., Yoerger, D., Giere, O., Kuever, J., Marbler, H., Mawick, J., Mertens, C., Stöber, U., Walter, M., Paulick, H., Peters, M., Strauss, H., Sander, S., Stecher, J., Warmuth, M., Weber, S., Ostertag-Henning, C., 2007. Young volcanism and related hydrothermal activity at 5°S on the slow-spreading southern Mid-Atlantic Ridge. Geochemistry, Geophys. Geosystems 8, 1–17. https://doi.org/10.1029/2006GC001509

Han, X., Wu, G., Cui, R., Qiu, Z., Deng, X., Wang, Y., 2010. Discovery of a Hydrothermal Sulfide Deposit on the Southwest Indian Ridge at 49.2°E. AGU fall Meet. Abstr., https://abstractsearch.agu.org/meetings/2010/FM/OS21C-1531.html.

Li, J., Jian, H., Chen, Y.J., Singh, S.C., Ruan, A., Qiu, X., Zhao, M., Wang, X., Niu, X., Ni, J., 2015. Seismic observation of an extremely magmatic accretion at the ultraslow spreading Southwest Indian Ridge. Geophys. Res. Lett. 42, 2656–2663.

Liao, S., Tao, C., Li, H., Barriga, F.J.A.S., Liang, J., Yang, W., Yu, J., Zhu, C., 2018. Bulk geochemistry, sulfur isotope characteristics of the Yuhuang-1 hydrothermal field on the ultraslow-spreading Southwest Indian Ridge. Ore Geol. Rev. 96, 13–27. https://doi.org/10.1016/j.oregeorev.2018.04.007

Liao, S., Tao, C., Zhu, C., Li, H., Li, X., Liang, J., Yang, W, Wang, Y., 2019. Two episodes of sulfide mineralization at the Yuhang-1 hydrothermal field on the Southwest Indian Ridge: Insight from Zn isotopes. Chem. Geol. 507, 54-63.

Lowell, R.P., 2010. Hydrothermal Circulation at Slow Spreading Ridges : Analysis of Heat Sources and Heat Transfer Processes, in: Diversity of Hydrothermal Systems on Slow Spreading Ocean Ridges. pp. 11–26.

Macdonald, K.C., 1998. Linkages Between Faulting , Volcanism , Hydrothermal Activity and Segmentation on Fast Spreading Centers, in: Faulting and Magmatism at Mid-Ocean Ridges. pp. 27–58.

Marcon, Y., Sahling, H., Borowski, C., dos Santos Ferreira, C., Thal, J., Bohrmann, G., 2013. Megafaunal distribution and assessment of total methane and sulfide consumption by mussel beds at Menez Gwen hydrothermal vent, based on geo-referenced photomosaics.

Deep. Res. Part I Oceanogr. Res. Pap. 75, 93–109. https://doi.org/10.1016/j.dsr.2013.01.008

McCaig, A.M., Cliff, R.A., Escartin, J., Fallick, A.E., MacLeod, C.J., 2007. Oceanic detachment faults focus very large volumes of black smoker fluids. Geology 35, 935–938. https://doi.org/10.1130/G23657A.1

McCaig, A.M., Delacour, A., Fallick, A.E., Castelain, T., Früh-green, G.L., 2010. Detachment Fault Control on Hydrothermal Circulation Systems : Interpreting the Subsurface Beneath the TAG Hydrothermal Field Using the Isotopic and Geological Evolution of Oceanic Core Complexes in the Atlantic, in: Diversity of Hydrothermal Systems on Slow Spreading Ocean Ridges. pp. 207–239.

Mendel, V., Sauter, D., Parson, L., Vanney, J.-R., 1997. Segmentation and Morphotectonic Variations Along a Super Slow-Spreading Center: The Southwest Indian Ridge (57° E-70° E). Mar. Geophys. Res. 19, 505–533.

Niu, X., Ruan, A., Li, J., Minshull, T.A., Sauter, D., Wu, Z., Qiu, X., Zhao, M., Chen, Y.J., Singh, S., 2015. Along-axis variation in crustal thickness at the ultraslow spreading Southwest Indian Ridge (50°E) from a wide-angle seismic experiment. Geochemistry, Geophys. Geosystems 16, 468–485. https://doi.org/10.1002/2014GC005645

Ondréas, H., Fouquet, Y., Voisset, M., Radford-Knoery, J., 1997. Detailed Study of Three Contiguous Segments of the Mid-Atlantic Ridge, South of the Azores (37° N to 38°30′ N), Using Acoustic Imaging Coupled with Submersible Observations. Mar. Geophys. Res. 19, 231–255. https://doi.org/10.1023/A:1004230708943

Sauter, D., Cannat, M., Meyzen, C., Bezos, A., Patriat, P., Humler, E., Debayle, E., 2009. Propagation of a melting anomaly along the ultraslow Southwest Indian Ridge between 46 ◦ E and 52 ◦ 20 E : interaction with the Crozet hotspot ? Geophys. J. Int. 179, 687–699. https://doi.org/10.1111/j.1365-246X.2009.04308.x

Son, S., Moon, J., Basset, D., Watts, A., 2014. Tectonic andmagmatic control of hydrothermal activity along the slow-spreading Central Indian Ridge, 8°S–17°S. Geochemistry Geophys. Geosystems 15, 2011–2020. https://doi.org/10.1002/2013GC005206.Received

Tao, C., Li, H., Jin, X., Zhou, J., Wu, T., He, Y., Deng, X., Gu, C., Zhang, G., Liu, W., 2014. Seafloor hydrothermal activity and polymetallic sulfide exploration on the southwest Indian ridge. Chin. Sci. Bull. 59, 2266–2276.

Tao, C., Lin, J., Guo, S., Chen, Y.J., Wu, G., Han, X., German, C.R., Yoerger, D.R., Zhou, N., Li, H., 2012. First active hydrothermal vents on an ultraslow-spreading center: Southwest Indian Ridge. Geology 40, 47–50.

Tao, C., Wu, G., Ni, J., Zhao, H., Su, X., Zhou, N., Li, J., Chen, Y. J., Cui, R., Deng, X., Egorov, I., Dobresova, I. G., Sun, G., Qiu, Z., Deng, X., Zhou, J., Gu, C., Li, J., Yang, J., Zhang, K., 2009; New hydrohtermal fields found along the SWIR during the Legs 5-7 of the Chinese DY115-20 Expedition. AGU fall Meet. Abstr. https://abstractsearch.agu.org/meetings/2009/FM/OS21

Yang, A.Y., Zhao, T.P., Zhou, M.F., Deng, X.G., 2017. Isotopically enriched N-MORB: A new geochemical signature of off-axis plume-ridge interaction—A case study at 50°28′E, Southwest Indian Ridge. J. Geophys. Res. 122.

Yu, X. and Dick, H.J., 2020. Plate-driven micro-hotspots and the evolution of the Dragon

Flag melting anomaly, Southwest Indian Ridge. Earth Planet. Sci. Lett. 531, 116002.

Yue, X., Li, H., Ren, J., Tao, C., Zhou, J., Wang, Y., Lü, X., 2019. Seafloor hydrothermal activity along mid-ocean ridge with strong melt supply: study from segment 27, southwest Indian ridge. Sci. Rep. 9, 1–10. https://doi.org/10.1038/s41598-019-46299-1

Zhang, T., Lin, J., Gao, J.Y., 2013. Magmatism and tectonic processes in Area A hydrothermal vent on the Southwest Indian Ridge. Sci. China Earth Sci. 56, 2186–2197. https://doi.org/10.1007/s11430-013-4630-5

Zhao, M., Qiu, X., Li, J., Sauter, D., Ruan, A., Chen, J., Cannat, M., Singh, S., Zhang, J., Wu, Z., Niu, X., 2013. Three-dimensional seismic structure of the Dragon Flag oceanic core complex at the ultraslow spreading Southwest Indian Ridge (49°39′E). Geochemistry, Geophys. Geosystems 14, 4544–4563. https://doi.org/10.1002/ggge.20264

Figure captions

Figure 1. Location and bathymetry of the Southwest Indian Ridge. Red circles indicate confirmed hydrothermal venting fields and yellow circles represent inferred hydrothermal venting fields from the InterRidge database (http://vents-data.interridge.org). Black circles mark the location of mantle hotspots. The shaded area marks the study area between the Indomed and Gallieni fracture zones. The inset figure shows the global distribution of hydrothermal venting fields from GeoMapApp. (Created by Generic Mapping Tools (GMT version 5), from http://gmt.soest.hawaii.edu/. The topography data is from https://www.ngdc.noaa.gov/mgg/global/.)

Figure 2. Bathymetry, segmentation, and known or inferred vent fields of the study area. (Created by Generic Mapping Tools (GMT version 5), from http://gmt.soest.hawaii.edu/. The topography is from multibeam sonar data by Chinese Dayang cruises. The resolution of the bathymetry grid is 50m)

Figure 3. (a) Areal bathymetry and hydrothermal vent field distribution for segment 28. The red dotted line is the location of line showing on Figure 4. (b) Cross-sections through the vent field locations. (Created by Generic Mapping Tools (GMT version 5), from http://gmt.soest.hawaii.edu/. The topography is from multibeam sonar data by Chinese Dayang cruises, with bathymetry grid 50m.)

Figure 4. Horizontal and vertical distribution of ΔNTU along the DHDS line through Longqi-2, including ORP data from the tow body. Note prominent ORP anomalies near 37°52.4' and 37°52.8'S. (a) Created by Ocean Data View (ODV) (Schlitzer, R., Ocean Data View, odv.awi.de, 2018).

Figure 5. (a) Areal bathymetry and hydrothermal vent field distribution for segment 29. The red dotted line is the location of line showing on Figure 6. (b) Cross-sections through the vent field locations. (Created by Generic Mapping Tools (GMT version 5), from http://gmt.soest.hawaii.edu/. The topography is from multibeam sonar data by Chinese Dayang cruises, with bathymetry grid 50m.)

Figure 6. Horizontal and vertical distribution of ΔNTU along the DHDS line through Yuhuang hydrothermal field. (a) Created by Ocean Data View (ODV) (Schlitzer, R., Ocean Data View, odv.awi.de, 2018).

Figure 7. Horizontal and vertical distribution of ΔNTU along the DHDS line through Yuhuang hydrothermal field -2. (a) Created by Ocean Data View (ODV) (Schlitzer, R., Ocean Data View, odv.awi.de, 2018).

Figure 8. (a) Areal bathymetry and hydrothermal vent field distribution for segment 30. The red dotted line is the location of line showing on Figure 8. (b) Cross-sections through the vent field locations. (Created by Generic Mapping Tools (GMT version 5), from http://gmt.soest.hawaii.edu/. The topography is from multibeam sonar data by Chinese Dayang cruises, with bathymetry grid 50m.)

Figure 9. Horizontal and vertical distribution of ΔNTU along the DHDS line through S30 hydrothermal field..

(a) Created by Ocean Data View (ODV) (Schlitzer, R., Ocean Data View, odv.awi.de, 2018).

Figure 10. Global trend of vent field spatial density (F_s) vs. spreading rate along OSRs. Red line is linear regression trend (y=0.027x + 0.72) using only the blue circles (ridge sections using data from the InterRidge Database), grey lines are ±95% confidence band. Red star denotes results from this paper. Yellow squares refer to segments with detailed surveys using NTU and Oxidation-Reduction Potential sensors: eastern Galápagos Spreading Center (eGSC), central Galápagos Spreading Center (cGSC,), Eastern Lau Spreading Center (ELSC), and Northern East Pacific Rise (NEPR) (Baker, 2017), and segment 27 (S27) (Yue et al., 2019). The figure is modified from Beaulieu et al. (2015) and Baker (2017).

Figure 11. Schematic distribution of known or inferred active vent fields on (a) a strongly magmatic segment and (b) a weakly magmatic segment in our study area.

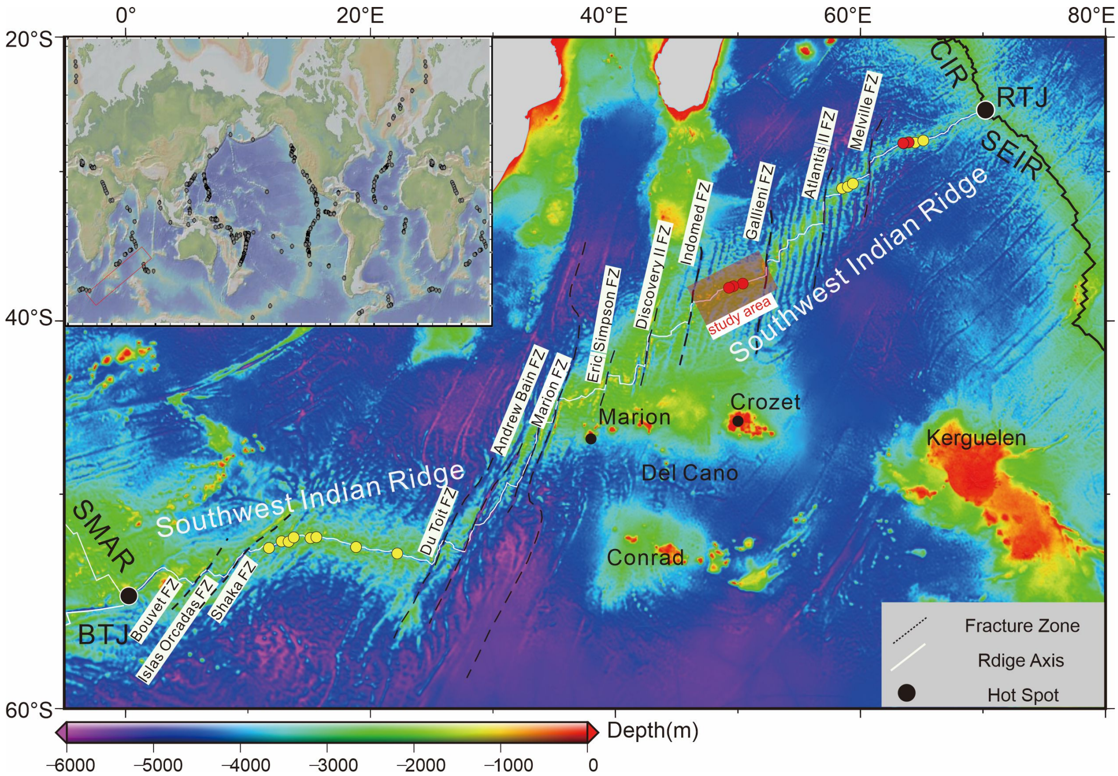

Figure 1

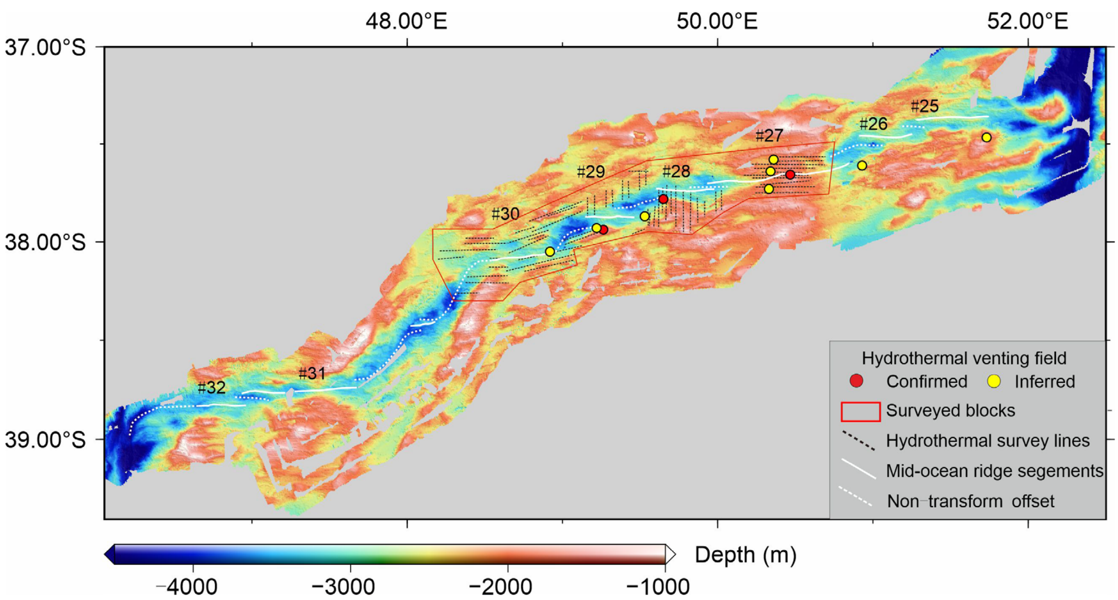

Figure 2

486 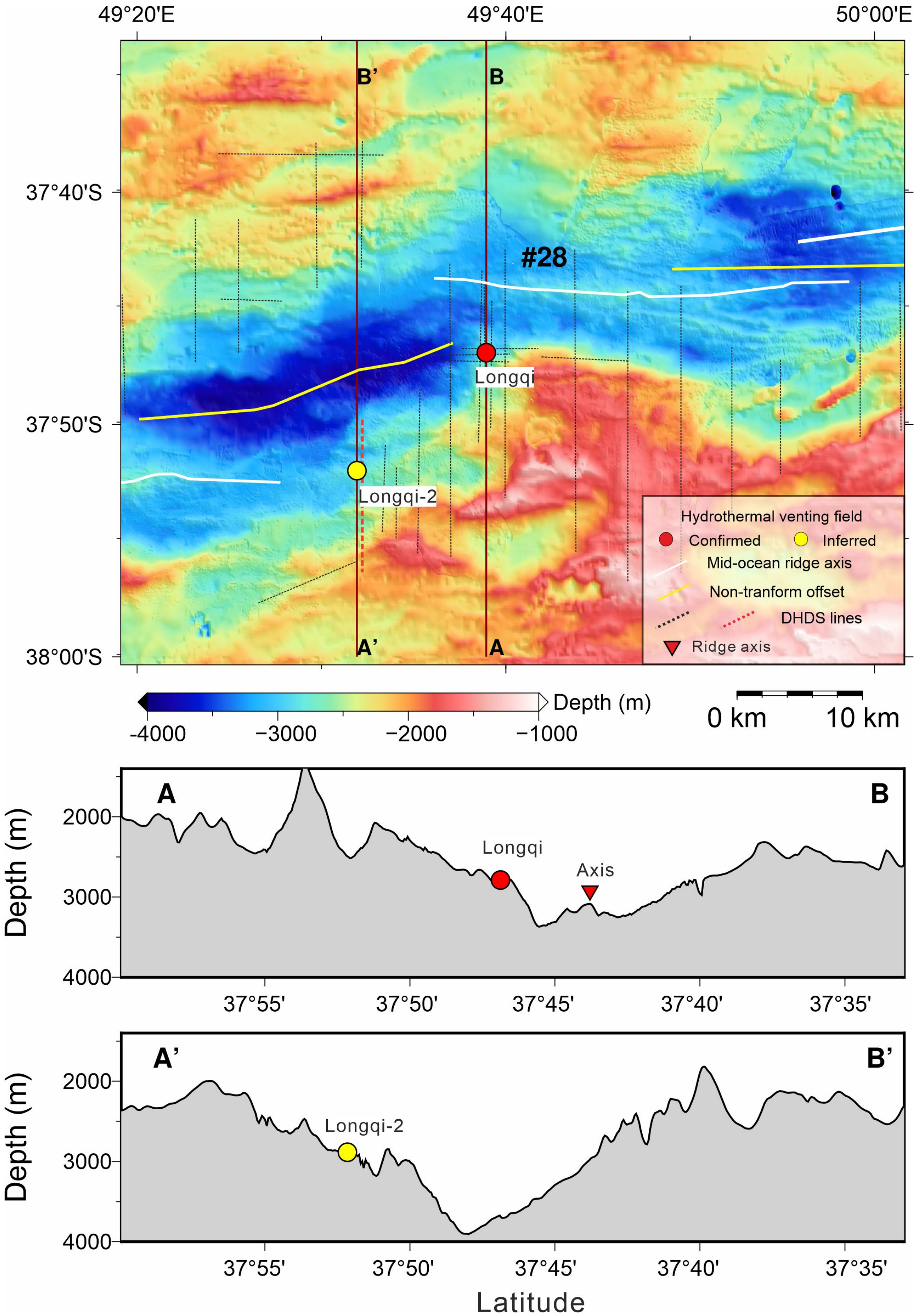

487 Figure 3

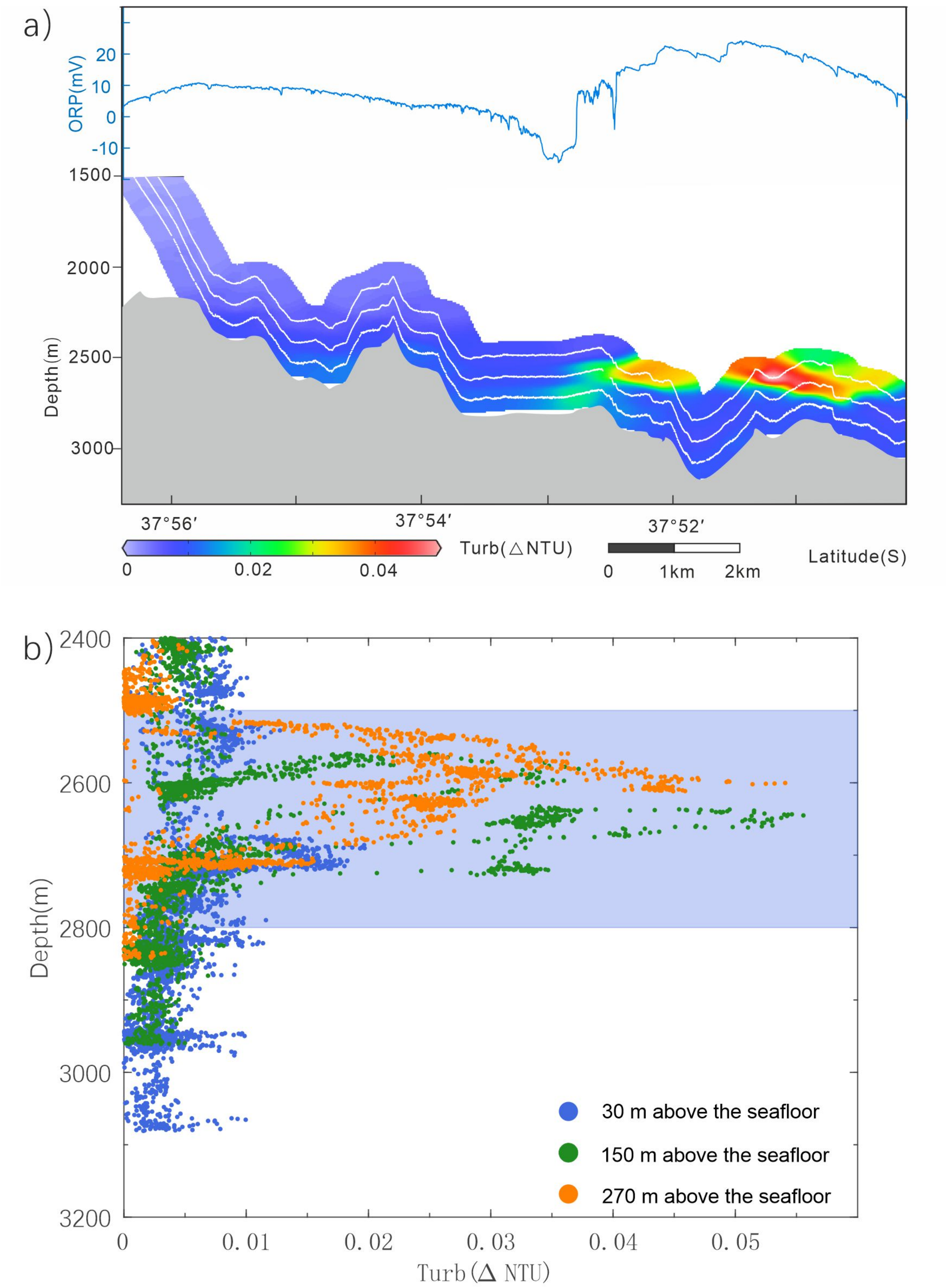
a)
ORP(mV)
20
10
0
-10
1500
2000
2500
3000
Depth(m)
37°56′
37°54′
37°52′
Turb(△NTU)
0
0.02
0.04
0
1km
2km
Latitude(S)
b)
2400
2600
2800
3000
3200
Depth(m)
0
0. 01
0. 02
0. 03
0. 04
0. 05
Turb(Δ NTU)
30 m above the seafloor
150 m above the seafloor
270 m above the seafloor

Figure 4

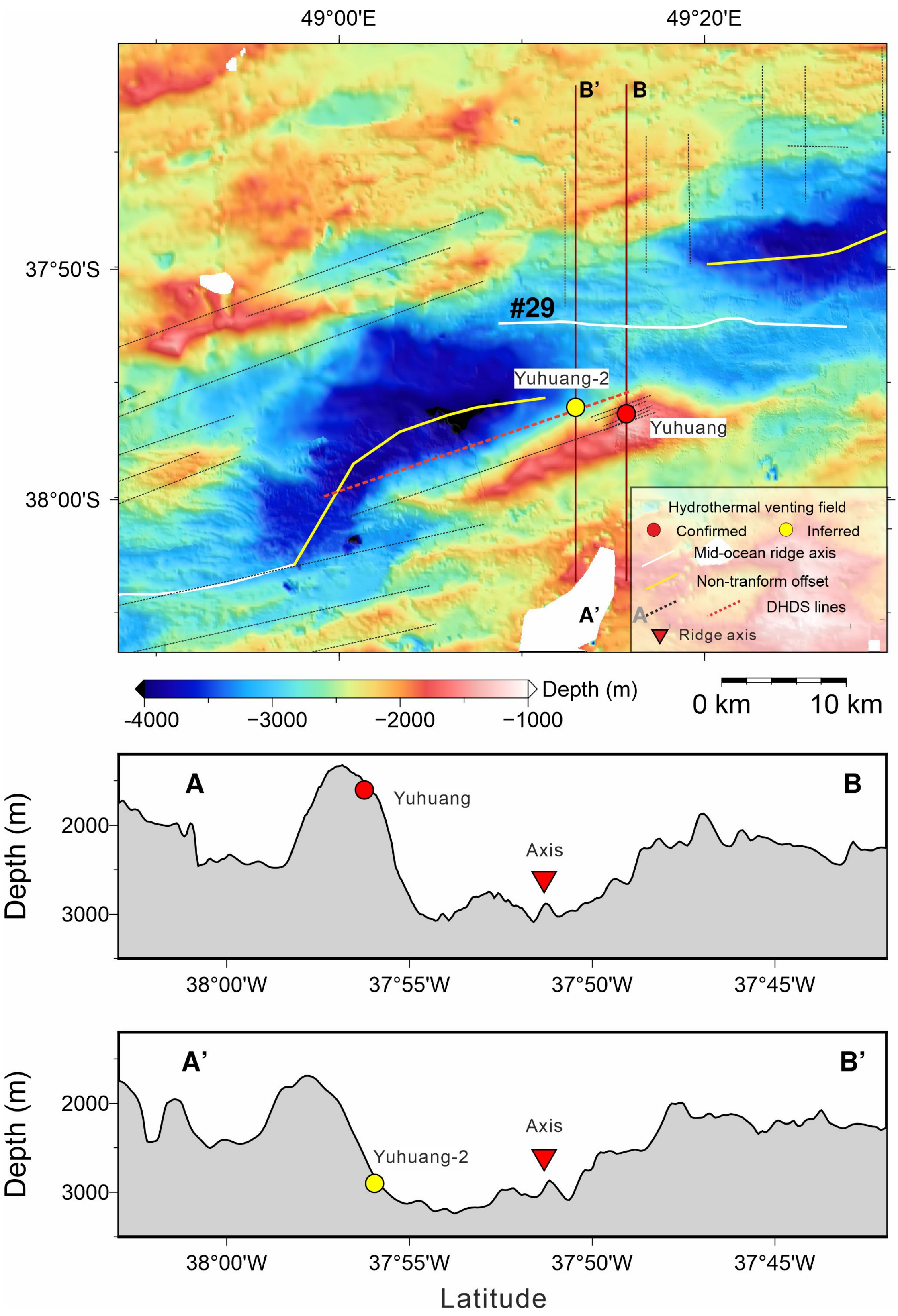

49°00'E
49°20'E
37°50'S
38°00'S
B'
B
#29
Yuhuang-2
Yuhuang
A'
A
Hydrothermal venting field
Confirmed
Inferred
Mid-ocean ridge axis
Non-tranform offset
DHDS lines
Ridge axis
Depth (m)
-4000
−3000
−2000
−1000
0 km
10 km
Depth (m)
2000
3000
A
B
Yuhuang
Axis
38°00'W
37°55'W
37°50'W
37°45'W
A'
B'
Yuhuang-2
Axis
Latitude

Figure 5

494

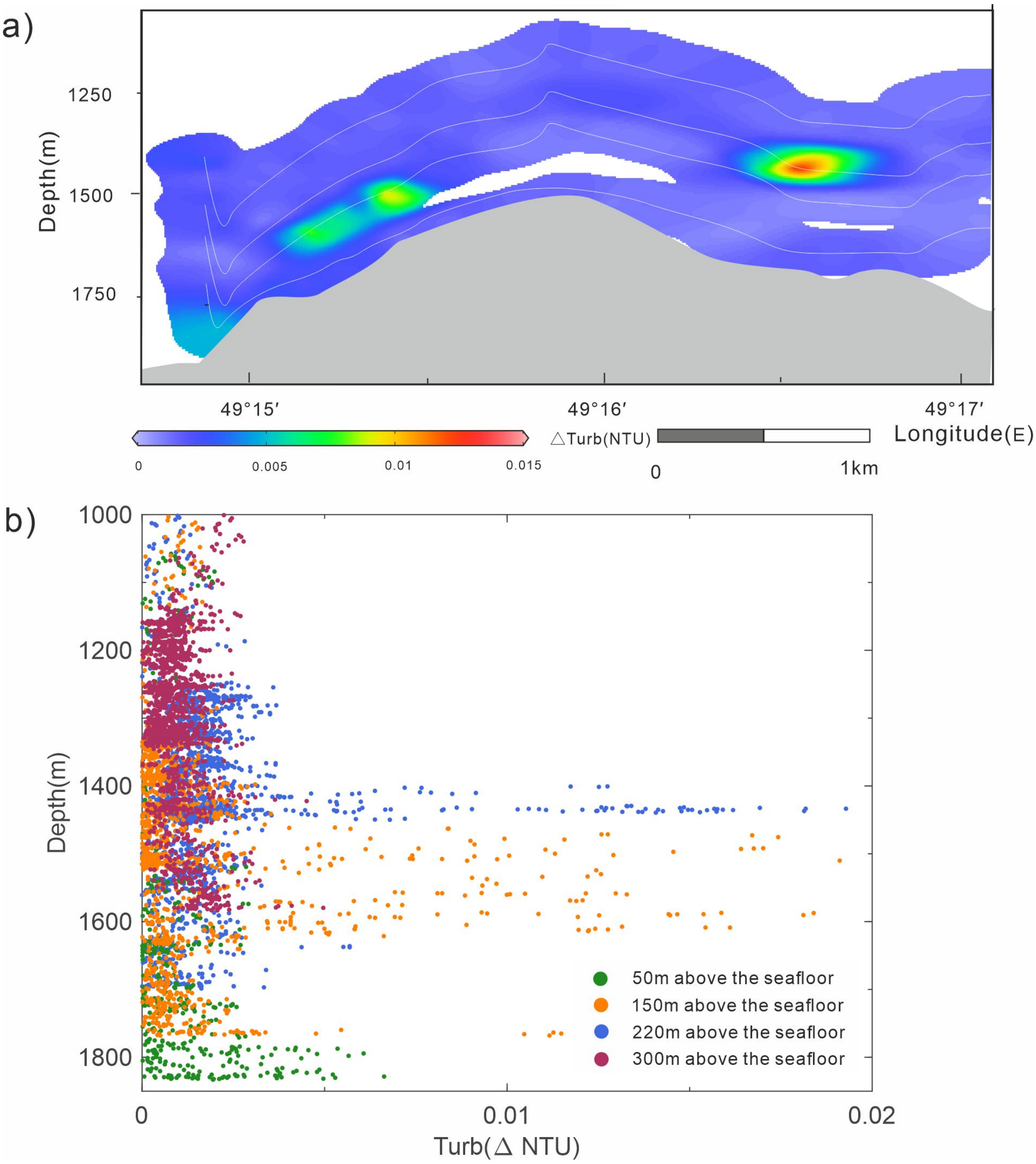

495

496 Figure 6

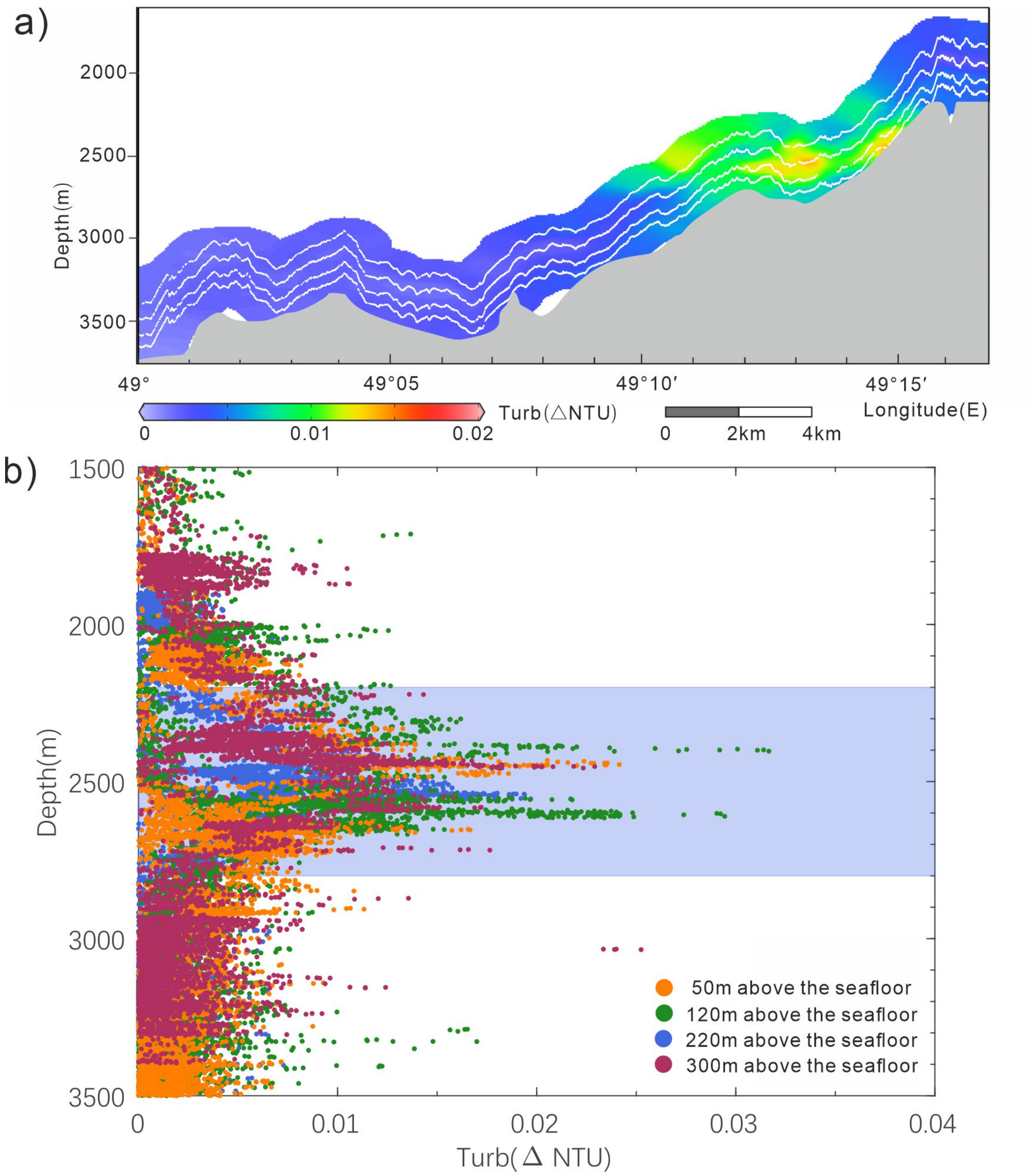
a)
Depth(m)
2000
2500
3000
3500
49°
49°05
49°10′
49°15′
Longitude(E)
Turb(△NTU)
0
0.01
0.02
0
2km
4km
b)
1500
2000
2500
3000
3500
Depth(m)
0
0.01
0.02
0.03
0.04
Turb(Δ NTU)
50m above the seafloor
120m above the seafloor
220m above the seafloor
300m above the seafloor

Figure 7

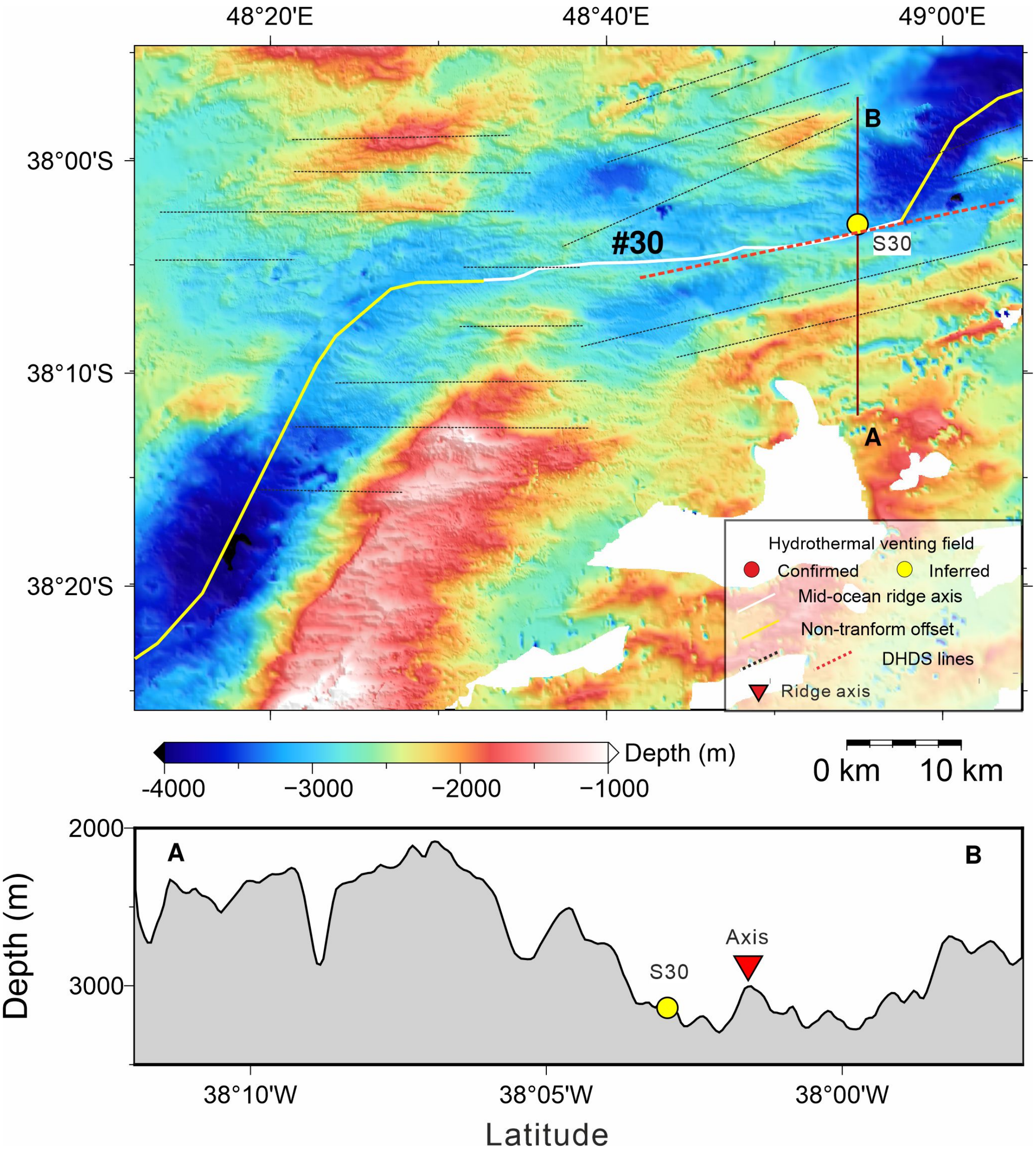

499

500 Figure 8

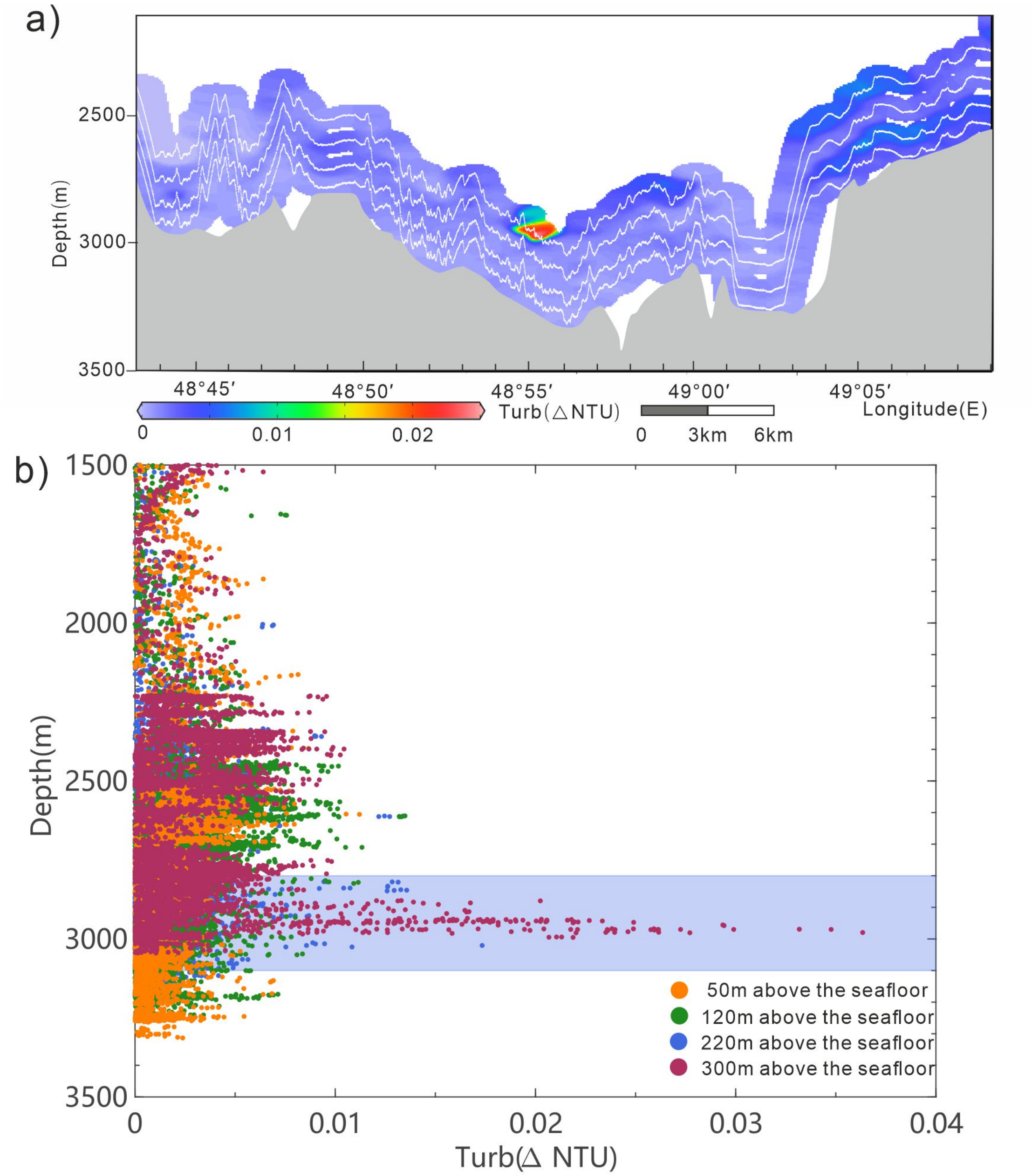
a)
2500
3000
3500
Depth (m)
48°45′
48°50′
48°55′
49°00′
49°05′
Longitude(E)
0
0.01
0.02
Turb(△NTU)
0
3km
6km
b)
1500
2000
2500
3000
3500
Depth(m)
0
0.01
0.02
0.03
0.04
Turb(Δ NTU)
50m above the seafloor
120m above the seafloor
220m above the seafloor
300m above the seafloor

Figure 9

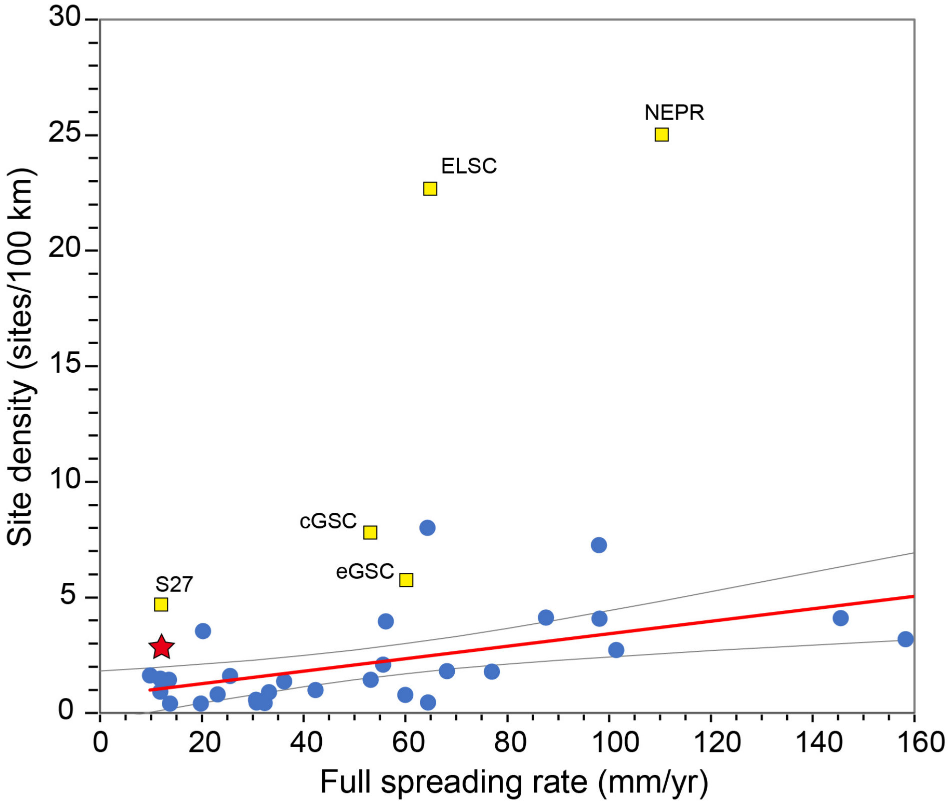
NEPR
ELSC
cGSC
eGSC
S27
Site density (sites/100 km)
Full spreading rate (mm/yr)
0
5
10
15
20
25
30
0
20
40
60
80
100
120
140
160

Figure 10

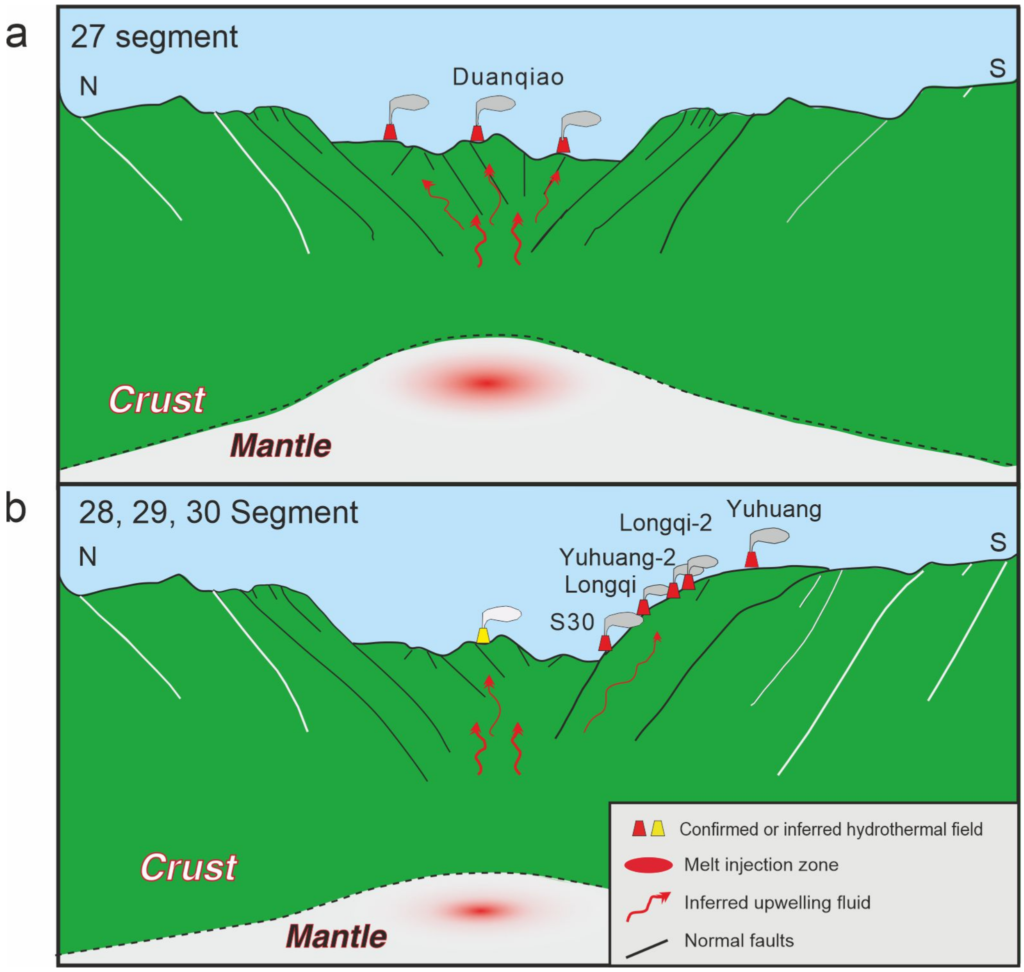
a
27 segment
N
Duanqiao
S
Crust
Mantle
b
28, 29, 30 Segment
N
Longqi-2
Yuhuang
Yuhuang-2
Longqi
S30
S
Crust
Mantle
Confirmed or inferred hydrothermal field
Melt injection zone
Inferred upwelling fluid
Normal faults